Journal of Data Science and Modeling, Vol. 3, No. 1, 49-78, December 2024

Research Manuscript

Unsteady numerical simulation and data analysis of hysteresis associated with water uptake in capillary tube

Farnood Freidooni*, Ali Rajabpour[1], Sina Nasiri[1]

[1] Mechanical Engineering Department, Imam Khomeini International University, Qazvin, 34148-96818, Iran

Recieved: 30/09/2025 Accepted: 06/12/2025

Abstract: Capillary action and water uptake are essential phenomena with broad applications in industrial, medical, and agricultural systems. This study presents a detailed numerical investigation and statistical data sampling of capillary rise, accounting for hysteresis effects associated with density, surface tension, contact angle, gravity, tube diameter, and inclination. The selected domain includes 1 mm and 5 mm capillary tubes. A pressure-based, time-dependent, incompressible Newtonian solver is employed using the finite-volume method on a co-located grid with algebraic multigrid acceleration and MPI parallelization. Pressure–velocity coupling is handled through the PISO algorithm. Results indicate that increasing tube diameter or surface tension enhances uptake velocity by 98–100% and reduces filling time by 49–50%, with only minor inertial/dissipative deviations (1–12%). Contact angle strongly affected rise dynamics, nearly doubling filling time, while gravity produced marginal delays with negligible meniscus impact. Inclined tubes (45°) exhibited transient meniscus asymmetry due to contact-angle differences, yet overall filling duration remained comparable to vertical and horizontal configurations.

Keywords: Numerical Modeling, Capillary Action, Statistical Data Sampling, Fluid Dynamics.

Mathematics Subject Classification (2010): 76D05, 76A20.

*Corresponding Author: F.freidooni@alumni.iut.ac.ir

1. Introduction

Capillary flow phenomena, specifically the uptake of fluids within capillary tubes (CTs), constitute a fundamental and widely applicable problem in fluid mechanics, materials science, life sciences, and numerous industries, ranging from refrigeration to space technologies. These include angiogenesis (Dremin et al. , 2025), water and nutrient transport in plants through root uptake, xylem, and leaf transpiration (Folch , 2025), targeted drug delivery to cancer cells (Li et al. , 2021), water purification (Fadel , 2014), leachate separation in waste management, nutrient supply to human hair (Martic et al. , 2002), among others. Recently, with advancements in molecular dynamics simulations, the study and computational modeling of capillary action in micro- and nano- tubes at the micro- and nanoscale has attracted considerable attention (Martic et al. , 2002; Joly , 2011; Amarasinghe et al. , 2014; Zhang et al. , 2022). On the other hand, theoretical models such as the Lucas-Washburn equation (L-W) (Washburn , 1921), Bosanquet equation (Bosanquet , 1923; Chen and Zhou , 2023), Quere equation ($h = \sqrt{\frac{2\gamma cos\theta}{\rho R}t}$, where the γ, θ, ρ, and t are surface tension, contact angle, fluid density, and time, respectively. (Quéré , 1997; Quéré et al. , 1999), Fries and Dreyer model ($h = \frac{2\gamma cos\theta}{\rho g R}\left[1 + W\left(-e^{-1-\frac{\rho^2 g^2 R^3}{16\eta\gamma cos\theta}t}\right)\right]$, where W and η are the Lambert function and fluid viscosity) (Fries and Dreyer , 2008), and Jurin's law (Jurin , 1718, 1719) have been proposed to predict capillary phenomena, each relying on simplifying assumptions and neglecting less influential parameters. Bosanquet equation (see eq. 1.1) considers inertial and viscous forces by:

$$h = \sqrt{\frac{R\gamma cos\theta}{2\eta}\left[t - \frac{R^2\rho}{8\eta}\left(1 - e^{-\frac{8\eta}{R^2\rho}t}\right)\right]} \tag{1.1}$$

If the $t \to \infty$, this equation approaches the L-W equation. Each of these equations have a specific efficiency in specific conditions of the flow regime, which are: the L-W equation in the purely viscous stage, the Bosanquet equation in the viscous and inertial stage, Quere in the early stage of low-viscosity fluid, Fries and Dreyer model in the viscous and gravitational stage. However, to the best of the authors' knowledge, computational fluid dynamics (CFD) studies of capillary dynamics in millimeter-scale tubes have received relatively little attention in the literature (e. g. Adibifard et al. (2020). Several factors, such as tube diameter, cross-section shape (Legait , 1983; Kubochkin and Gambaryan-Roisman , 2022), surface tension, contact angle, fluid properties (i. e. density), tube inclination angle, and gravitational force have a significant impact on the observed dynamic capillary effect (Koźluk et al. , 2025).

A profound understanding and accurate modeling of capillary phenomena ne-

cessitate considering the complex interplay of capillary, viscous, gravitational (or microgravity), surface tension, contact angle, inertia, and surface geometry forces. Significant advancements in CFD methods over the past two decades have enabled more precise numerical simulations and deeper insights into the governing mechanisms of these flows. This research background examines the evolutionary trajectory of theoretical models, numerical challenges, and achievements in CFD simulation within this domain.

The cornerstone of our understanding of capillary flow rests primarily on the well-established L-W equation (Washburn , 1921; Lucas , 1918) according to eq. 1.2. This equation:

$$\frac{dh}{dt} = \frac{\Delta P \ \left(R^2 + 4\varepsilon R\right)}{8\eta h} \ ; \ \begin{cases} \Delta P = \frac{2\gamma cos\theta}{R} : \ from\ Yang - Laplace\ equiation \\ \varepsilon \ : slip\ coefficient \end{cases}$$

$$\rightarrow h\left(t\right) = \sqrt{\frac{2\gamma R cos\theta}{2\eta}}\sqrt{t} \tag{1.2}$$

Describes capillary imbibition in an ideal cylindrical CT of constant circular cross-section for incompressible Newtonian fluids, illustrating the role of capillary force in overcoming viscous resistance to induce upward flow (against gravity) or lateral penetration (Cai et al. , 2021). The gravity force should be neglected in horizontal cylindrical CTs, or if the uptake height is small enough. However, inherent limitations of this classical model, particularly when confronted with complex geometries (such as non-circular tubes, varying cross-sections, parallel plates, heterogeneous porous media), rough surfaces, inertial effects, and dynamic contact angles, have spurred the development of numerous modified and extended models. Cai et al. (2021), in a comprehensive review, highlighted recent progress in generalizing the L-W equation to non-uniform and non-circular channels, fractures, non-straight tubes, and heterogeneous porous media, confirming the critical need for more powerful numerical methods to simulate these complex scenarios accurately.

Efforts to overcome the limitations of simplified models have led to the emergence of more complex and physically grounded formulations. Bullard and Garboczi (2009) employed the principle of free energy minimization and variational principles to develop a comprehensive model for calculating the equilibrium height and meniscus shape of a liquid column between two closely spaced parallel plates. Their analysis derived the Euler-Lagrange equation governing the meniscus shape and precise boundary conditions at the three-phase junction, confirming the validity of the Young-Dupré equation for the thermodynamic contact angle in this configuration. They demonstrated that a generalized Laplace-Young equation provides exact prediction of the mean meniscus elevation at any wall separation. In contrast, the classical Laplace-Young equation for midpoint elevation is accurate

only as the separation approaches either zero or infinity. The development of these energy-based models paved the way for novel approaches. In a significant theoretical development, Caltagirone (2024) presented a new formulation for capillary flows on surfaces or at fluid-fluid interfaces, marking a fundamental step forward. This formulation is based on the Helmholtz-Hodge decomposition of the capillary acceleration into curl-free and divergence-free components: the gradient of the scalar potential of acceleration and the dual curl of the vector potential, respectively. Distinctive features of this formulation include: (1) definition of a directional curvature based on the dihedral angle instead of mean curvature, (2) introduction of an intrinsic anisotropic surface tension per unit mass (thereby excluding density from the capillary terms in the equation of motion), and (3) introduction of the concept of capillary potential (energy per unit mass). This energy-based approach leads to an equation of capillary motion for a surface without thickness, which can be integrated as a source term into the equation of motion for immiscible fluids.

Accurate numerical simulation of capillary flow, particularly near the three-phase contact line, has consistently faced numerous challenges. Schönfeld and Hardt (2009) clearly demonstrated that precise modeling of contact angle properties plays a vital role in simulating free-surface microflows. They emphasized that CFD results exhibit pronounced mesh dependence, partly inherent to the modeling approach because the (non-integrable) viscous stress divergence at the three-phase contact line is typically neglected in standard CFD simulations. Furthermore, the numerical description of contact angles within the Volume of Fluid (VOF) method is prone to artificial diffusion. They proposed introducing a macroscopic slip range combined with a localized body force near the contact line as an effective solution to address both issues. Gründing et al. (2020) compared four different numerical approaches for modeling liquid uptake between parallel plates: the Arbitrary Lagrangian-Eulerian (ALE) method (using the OpenFOAM solver interTrackFoam), a geometric Volume of Fluid (VOF) code (FS3D), an algebraic VOF method (using the OpenFOAM solver interFoam), and a Level Set approach (using the BoSSS platform). Their results showed excellent agreement among the different numerical implementations (except for minor quantitative deviations in the adapted interFoam solver). Still, the quantitative comparison between the full continuum mechanical solutions and the ODE reference model (including the classical model and an extended model incorporating a Navier slip boundary condition on the capillary walls along with a corrected stationary rise height) was found to be only reasonable, particularly in cases with increasing oscillations. This study highlighted the importance of the appropriate selection of numerical methods and parameters (such as slip length). Mark and Boyer (2020) investigated poten-

tial errors in CFD simulations of passive capillary-driven flow within channels of varying geometry. By comparing simulation results with theoretical analysis, they established the spatial domain of validity for the continuum model in related applications at very fine scales, representing a crucial step in determining the reliability of CFD predictions at these scales.

CFD simulation of capillary flow has been applied and validated across diverse specialized domains. Gaulke and Dreyer (2015) used Flow3D software to simulate capillary transport of liquid between parallel perforated plates under microgravity conditions, correlating the capillary transport capability with perforation diameter and plate porosity. They found acceptable agreement between experimental and numerical results. Liu et al. (2016) performed CFD simulations to investigate capillary-driven liquid uptake in cylindrical containers equipped with lateral vanes under space conditions, analyzing the influence of vane dimensions and quantity on flow characteristics, which is critical for orbital refueling technology. Abdul Aziz et al. (2014) presented a three-dimensional finite volume numerical method to evaluate the effect of pin-through-hole (PTH) shape on capillary flow behavior during the wave soldering process. They demonstrated that circular PTH pins enabled the fastest solder front advancement, while angle-edged PTH components increased filling time and produced uneven profiles. Simulation results were validated experimentally against a single circular pin. López et al. (2021) presented a novel CFD model for investigating the effect of capillary pressure on the retention behavior of granular material. Their model simulated the onset of liquid menisci at inter-particle contacts under varying hydraulic conditions and was validated against experimental saturation data for smooth glass beads saturated with silicon oil at various capillary pressures, demonstrating high accuracy in reproducing the granular material's retention behavior.

Understanding capillary rise behavior within rough structures presents a major challenge with broad applications. Panter et al. (2023) demonstrated that accurately predicting rough capillary rise necessitates coupling two wetting phenomena: capillary rise and hemiwicking. Their experiments, simulations, and theory revealed that this coupling challenges conventional understanding and intuitions of wetting and roughness. Key findings included: (1) the critical contact angle for hemiwicking becomes separation-dependent (such that hemiwicking can vanish even for highly wetting liquids), (2) rise heights for perfectly wetting liquids can differ between smooth and rough systems despite identical 0° contact angles, and (3) raised liquid volumes are substantially increased in rough compared to smooth systems. They presented the "Dual-Rise" model to predict all rise heights and volumes with quantitative accuracy, applicable to general roughness, liquids, and surface wettabilities. This work underscores the inherent complexity associated

with surface roughness, often overlooked in previous simplified models.

Capillary flow modeling plays a pivotal role in optimizing engineering systems such as vapor-compression refrigeration. Khunte and Mishra (2022) analyzed the flow of refrigerant R152a inside straight adiabatic CTs by developing a mathematical model and utilizing ANSYS CFX. Their model predicted the required length and diameter of the adiabatic straight CT for a given mass flow rate, with results showing fair agreement with CFX simulations. Similarly, Bhangale and Deshmukh (2021) focused on improving vapor-compression refrigeration system performance through optimal CT design, studying the results for straight and helical CTs using CFD analysis across various lengths and diameters to determine the optimal size. These studies highlight the importance of CFD simulation in the effective design of critical components reliant on capillary flow.

The present research background illustrates a significant evolution in the modeling and CFD simulation of capillary rise phenomena in tubes. The progression from simplified analytical models like Lucas-Washburn towards more complex formulations grounded in the first principles of continuum mechanics and thermodynamics (e.g., Bullard and Garboczi (2009); Caltagirone (2024)), coupled with the development and comparison of advanced numerical methods (VOF, ALE, Level Set) to overcome inherent challenges in capturing interfacial and contact line phenomena (Schönfeld and Hardt (2009), Gründing et al. (2020)), has led to a marked increase in simulation accuracy and reliability. The widespread validation of these models across a diverse array of complex applications, including space technology (Liu et al. , 2016), electronics manufacturing (Abdul Aziz et al. , 2014), geotechnical engineering (López et al. , 2021), and refrigeration system design (Khunte and Mishra , 2022; Bhangale and Deshmukh , 2021), attests to the relative maturity of this research field. Nevertheless, significant challenges persist. These include the need for more precise modeling of multi-scale surface roughness effects, particularly their influence on phenomena like hemiwicking (Panter et al. , 2023). Further advancements are required in modeling dynamic contact angles and inertial effects at micro-scales. Additionally, there is a pressing need to develop efficient multi-scale methods that can effectively couple molecular dynamics at interfaces with macroscopic continuum models, addressing issues related to the generalized Navier boundary condition and uncompensated Young stress. Finally, enhancing prediction accuracy in complex heterogeneous and multiphase systems remains a crucial area for future research. Future efforts will likely focus on developing more integrated formulations, leveraging machine learning for model and parameter optimization, and harnessing increasing computational power for more detailed three-dimensional simulations of realistic geometries. Achieving these objectives will enable more accurate prediction and control of capillary flows

in emerging applications, from advanced microfluidics to energy and biomedical technologies.

This work aims to bridge this gap by providing a detailed numerical investigation and statistical data sampling of capillary water uptake in such systems, considering the interplay of surface tension, contact angle, gravitational force, and tube inclination effects.

1.1 Research Objectives, Questions, AND Novelties

This research employs CFD techniques, numerical methods, and time-dependent statistical data sampling to simulate the capillary uptake of water in a CT. Consequently, the primary objective can be identified as elucidating the fluid dynamics governing the uptake motion of water in a CT. To achieve this objective, the fundamental question that must be addressed is: On which parameters does the fluid dynamics of capillary water uptake in a CT depend?

Therefore, it is imperative first to accomplish the micro-objectives of numerical model validation, investigation of grid independence, examination of time-step independence, identification of parameters influencing flow physics, and analysis of their effects. These objectives give rise to the following questions: To what extent does the implemented numerical model conform to the L-W equation? What constitutes the optimal time-step and computational grid size in terms of both computational accuracy and computational cost? Which parameters and through what mechanisms do they induce alterations in the fluid field behavior?

2. Methodology, Boundary Conditions, and Numerical Details

A summary of the overall workflow had been provided through Figure 1, in which the methodology employed in the study had been illustrated. After reviewing the literature, the process started with the mesh generation, including nearly 64000 mesh in a 5mm height and 1mm diameter CT. This is continued by time-dependent numerical simulations using a CFD code, where the internal flow is assumed to be laminar, constant properties, incompressible Newtonian flow at a Reynolds number below 1. During the solution process, a time-averaged statistical data sampling of all flow quantities, such as the velocity field, pressure field, and others, has been performed. The root-mean-square (RMS) values were also calculated and utilized to quantify statistical fluctuations. These values were updated at each time step. Throughout all these stages of the solution, the process was statistically in a steady state.

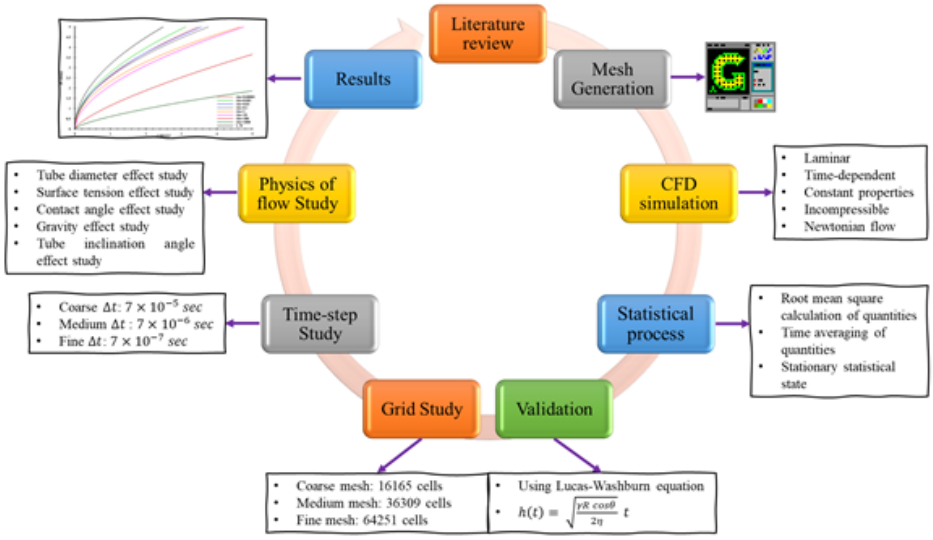

Figure 1: Workflow of the study, detailing the successive steps from literature review to results. The process contains mesh generation, CFD simulation, validation, grid, and time-step independence study, assessing the physics of flow, and presenting results.

The flow initial height is selected as $h_0 = 1mm$. Figure 2 represents the geometry and computational domain under consideration schematically. Cartesian coordinate system $(x,\ y)$ (the origin is shown in Figure 2) in which the x-direction is perpendicular to the tube axis (transversal) and the y-direction is aligned with the inflow direction (streamwise). The tube diameter and height are D and h, respectively. The initial fluid velocity was set to zero. Table 1 represents the case studies of the present study. Initially, an effort was made to ensure that the results obtained from CFD simulations within the CT align with the L-W equation. To this end, case studies involving variations in density were conducted to verify and validate the numerical simulation model. Subsequently, the grid independence study and the time-step independence study were conducted. Two tubes with inclination angles of 0 and 45 degrees have also been studied to investigate the effects of the inclination angle on the flow physics. On the other hand, to study the effect of the tube wall's shape (roughness) on the capillary phenomenon, five geometries—namely semi-rough, rough, sawtooth, sinusoidal wavy, and corrugated tubes—have been studied and investigated. The other parameter studies, which comprise a total of 30 simulations, are summarized in Table 1.

The governing equations of the flow are the Navier-Stokes equations, which include the continuity equation and the momentum equation, as described by

Table 1: Case studies description.

No.	$\rho\ \left(\frac{kg}{m^3}\right)$	Mesh quality	Time-step size	Description
1	0.00001	Fine	$7 \times 10^{-7}\ sec$	
2	0.001	Fine	$7 \times 10^{-7}\ sec$	These case studies are used
3	0.01	Fine	$7 \times 10^{-7}\ sec$	to capture the L-W equation
4	0.1	Fine	$7 \times 10^{-7}\ sec$	in CT by changing the
5	1	Fine	$7 \times 10^{-7}\ sec$	density of the fluid to
6	10	Fine	$7 \times 10^{-7}\ sec$	eliminate inertia effects
7	100	Fine	$7 \times 10^{-7}\ sec$	(see Figure 3).
8	1000	Fine	$7 \times 10^{-7}\ sec$	
9	0.001	Fine	$7 \times 10^{-7}\ sec$	64251 cells
10	0.001	Medium	$7 \times 10^{-7}\ sec$	36309 cells (Grid independence study)
11	0.001	Coarse	$7 \times 10^{-7}\ sec$	16165 cells
12	0.001	Fine	Fine	$\Delta t_I = 7 \times 10^{-7}\ sec$ (Time-step independence study)
13	0.001	Fine	Medium	$\Delta t_{II} = 7 \times 10^{-6}\ sec$
14	0.001	Fine	Coarse	$\Delta t_{III} = 7 \times 10^{-5}\ sec$
15	1000	Fine	Fine	$D = 0.5\ mm$
16	1000	Fine	Fine	$D = 1\ mm$ (Diameter study)
17	1000	Fine	Fine	$D = 2\ mm$
18	1000	Fine	Fine	$\gamma = 36.25\ mN/m$
19	1000	Fine	Fine	$\gamma = 72.5\ mN/m$ (Surface tension study)
20	1000	Fine	Fine	$\gamma = 145\ mN/m$
21	1000	Fine	Fine	$\theta = 30^\circ$
22	1000	Fine	Fine	$\theta = 55^\circ$ (Contact angle study)
23	1000	Fine	Fine	$\theta = 75^\circ$
24	1000	Fine	Fine	$\beta = 45^\circ$ (Inclination angle study)
25	1000	Fine	Fine	$\beta = 0^\circ$

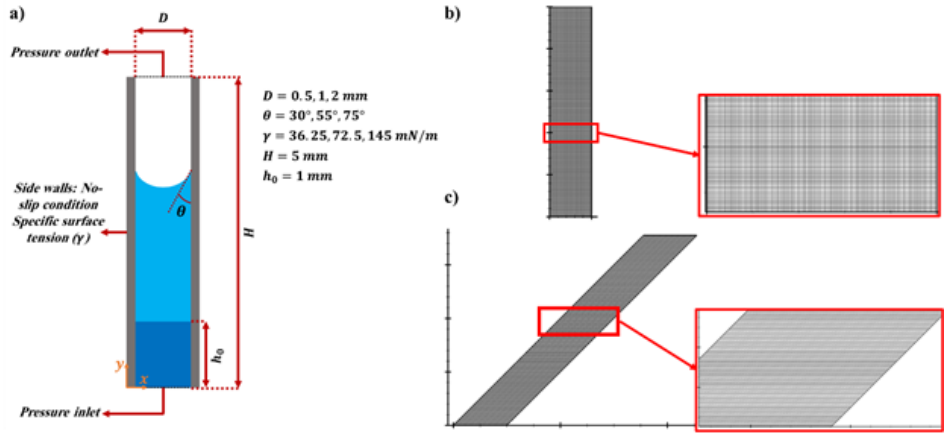

Figure 2: (a) The schematic view of the problem under consideration, boundary conditions, and dimensions; (b, c) computational grid and zoomed area of vertical CT (b) and inclined CT (c).

Equations 2.3 and 2.4:

$$\frac{D\rho}{Dt} + \rho \nabla . v = 0 \tag{2.3}$$

$$\rho \frac{Dv}{Dt} = -\nabla P + \mu \nabla^2 v + F \tag{2.4}$$

In these equations, $\frac{D}{Dt}$ is the material derivative, μ is the viscosity, ρ is the density, P is the pressure, t is time, v is the velocity, and F represents other forces.

The boundary condition at the inlet and the outlet of the tube is considered as the inlet and outlet gauge pressures, respectively, both set to zero. The lateral walls of the tube are defined as impermeable walls with no-slip condition and a specified surface tension of 72 mN/m. The contact angle between the fluid and the tube wall is 55° (the study of parameters i. e. surface tension, contact angle, gravitational force effect, and tube diameter will be discussed comprehensively later). The dynamic viscosity of the fluid was set to 0.001 $Pa.s$. The global Fredrich-Courant-Levy number was kept below 0.03 in all simulations.

The pressure-based solver is selected, and a time-dependent simulation is utilized. The flow field is selected as incompressible, constant properties, Newtonian homogeneous fluid. The finite volume method on a co-located grid system is used to discretize and solve the governing equations. The code uses a multigrid scheme to accelerate the solver's convergence by computing corrections on a series of coarse grid levels (Freidooni et al. , 2021, 2024). The use of this multigrid scheme tremendously reduces the number of iterations and the CPU time required to obtain a converged solution (Weiss et al. , 1997; Ubbink and Issa , 1999; Stüben

, 2001; Krajnović , 2011; Ziarani et al. , 2023). Accordingly, the computational processing is done with a computer consisting of a 26-core Intel CPU and 2 GB RAM for each one to solve the flow field at each time step.

The algebraic multigrid (AMG) method using the F-cycle for pressure and the flexible-cycle for x-, y-momentum is used. The absolute convergence criterion of residuals was 10^{-6} and 10^{-8} for the continuity and the x- and y-momentum equations, respectively. The parallelized code with commands from the message passing interface (MPI) library is used to carry out the simulations in a reasonable time. The bisection algorithms are used for partitioning (Freidooni et al. , 2024). The pressure and velocity fields were coupled using the PISO algorithm. Temporal discretization was performed using the first-order implicit method, while spatial discretization for gradient, pressure, momentum, and volume fraction fields utilized the least square cell-based, modified body force weighted, second-order upwind, and Geo-Reconstruct algorithms, respectively. The gravitational force is neglected in all cases.

2.1 Validation of numerical results

According to 1, eight case studies with fluid density variations ranging from 0.00001 to 1000 kg/m^3 were evaluated using a fine computational grid, and the fine time step. Figure 3 demonstrates the simulation results of fluid uptake in the CT vs L-W equation. The results of a fluid with a density of 0.001 kg/m^3, exhibit excellent and acceptable agreement with the L-W equation. This phenomenon confirms that eliminating the inertial effect in the CFD leads to matching the simulation results and the L-W equation. The deviation of the numerical results is noticeable from the beginning (Figure 3) and becomes increasingly significant over longer periods of the uptake process (longer fluid uptake time). This phenomenon occurs because, although the L-W equation was derived for Poiseuille flow, its formulation neglects inertial effects. Additionally, dissipative phenomena and other forces are not considered. To address these limitations, numerous modifications have been made to this equation in recent years, among which the Bosanquet equation (Krishna and van Baten , 2012; Chen and Zhou , 2023) stands out as one of the significant (Mu and Cao , 2024; Dimitrov et al. , 2007). In other words, to eliminate the effects of inertia and density in the numerical simulation by solely negating the fluid density parameter (while keeping other properties identical), the velocity and trend of CT filling exhibit excellent agreement with the L-W equation prediction, which indicates the validity of the numerical model. By increasing the density to the value of water's density, the results approach the realistic filling of the CT, which is demonstrated in Figure 3.

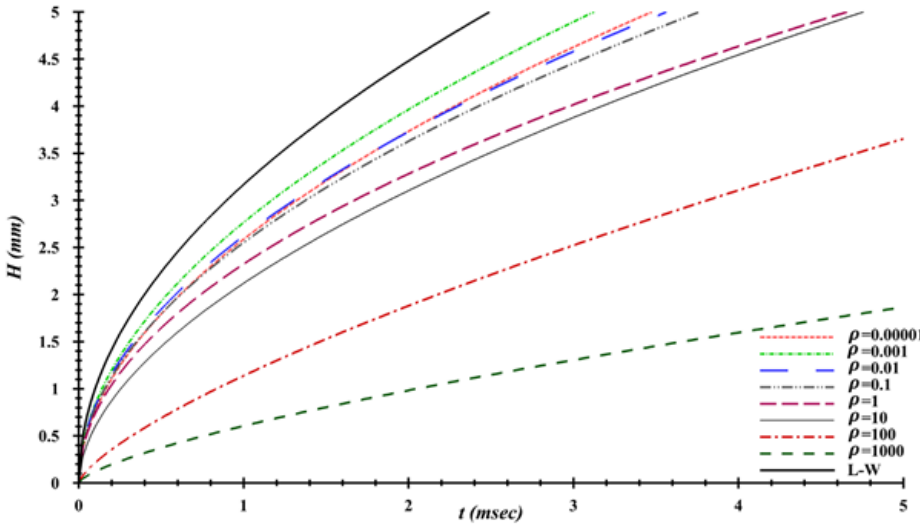

Figure 3: Fluid uptake in the CT with different fluid density (from 0.00001 to 1000 kg/m^3) via the L-W equation; vertical and horizontal axes are represented as mm (millimeter) and msec (millisecond).

2.2 Grid Study

In the previous section, the performance of the numerical model was validated using the L-W equation. In each numerical modelling, ensuring the independence of the final result from the computational grid is of critical importance. For this purpose, three computational grids were utilized. Furthermore, the smallest time step that maintains a Courant number below 0.03 was employed.

Three computational meshes containing 64251, 36309, and 16165 cells—referred to as fine, medium, and coarse, respectively—were evaluated according to Table 2.

Table 2: Grid study for CT for three different cases: fine, medium, and coarse.

Mesh	N	N_x	N_y	δ (mm)	Δ (mm)
Fine	64251	121	531	0.0083	0.0094
Medium	36309	91	399	0.0109	0.0125
Coarse	16165	61	265	0.0164	0.0189

The smallest distances from the wall (δ) in the fine and coarse meshes are (0.0083mm) and (0.0164mm), respectively. The largest distances from the wall (Δ) in the fine and coarse meshes are (0.0094mm) and (0.0189mm), respectively. Consequently, the mesh has been sufficiently refined to capture fine-scale fluid

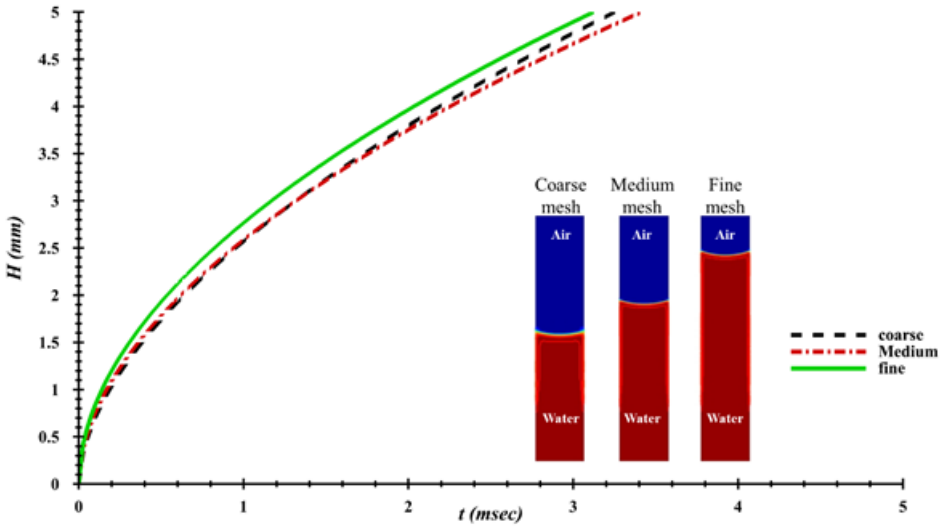

Figure 4: Grid study in CT (with fluid density of $0.001 kg/m^3$) for three different meshes: fine (64000), medium (32000), and coarse (16000); the vertical and horizontal axes are represented as mm (millimeter) and msec (millisecond).

phenomena. The computational grid orthogonality in both vertical and horizontal CTs has been implemented such that the grid remains perfectly orthogonal throughout the entire geometry. Consequently, skewness is minimized to the lowest possible value. The maximum aspect ratio of the cells is 1.5. In the inclined CT (45-degree), the minimum grid orthogonality is 70%. The examples of generated computational grids are depicted in Figure (2 (b, c)).

The results indicate that capillary action is relatively sensitive to the mesh, as noted by Schönfeld and Hardt (2009). This can be seen from Figure 4, where the coarse and medium meshes cause underpredicted results. The maximum difference between fine and medium mesh is on average 5%. The discrepancy between medium and coarse mesh is not significant. Based on the contours shown in Figure 4, near the tube walls for the coarse mesh case, the regions influenced by wall effects are not well simulated, and the gradients are perceived as more intense. Accordingly, the fine mesh was selected for subsequent analyses to ensure higher accuracy. The details of the meshes mentioned above are provided in Table 2.

2.3 Time-step study

Every time-dependent numerical simulation must be examined for time step independence, as shown in Table 1, three-time steps—$\Delta t = 7 \times 10^{-7}$, 7×10^{-6}, $7 \times 10^{-5} sec$—were evaluated within the CT, which had already been validated in

terms of grid independence and agreement with the L-W equation. The results indicate a relative sensitivity of the solution to the time step size. The discrepancies between the large to medium and medium to small time are nearly 10% and 3%, respectively. To ensure the results accuracy the fine time step ($\Delta t = 7 \times 10^{-7}\ sec$) is chosen.

3. Results and Discussion

Prior to discussing the investigation and study of the effects of parameters such as tube diameter, surface tension, contact angle, etc., on the phenomenon of capillary action and the water uptake within it, the fundamental physics of the flow in this case is first examined. The contours in Figure 5, which represent time-averaged data sampling statistics over the solution, show the mean velocity in the flow direction, mean velocity perpendicular to the flow direction, and mean static pressure. Since the tube wall is considered to be non-rough uniform surface, the velocity in the flow direction (Figure 5(a)) at a distance very close to the wall is nearly zero due to the no-slip condition. This condition remains constant and uniform along the entire length of the tube. The contour of velocity perpendicular to the flow direction (Figure 5(b)) indicates that, initially, during the upward movement from the initial height, the meniscus profile undergoes transitional changes. A sign of this is the presence of transverse velocities of equal magnitude and opposite signs, symmetric about the vertical axis of the tube. When the surface tension forces exerted by the walls reach equilibrium and balance, the transverse velocity tends to become negligible. However, at the end of the tube, this balance is disrupted again, and transverse velocities are observed. The mean static pressure contour (Figure 5(c)) also shows that the pressure is lower in magnitude at the beginning of the movement, increases in the middle section of the tube, and decreases again at the end of the path. The animation of water uptake in vertical capillary tube has been provided in the supplementary materials.

3.1 Tube diameter study

According to the L-W equation for capillary flow in a narrow (capillary) tube and assuming constant surface tension (γ), contact angle (θ), and fluid viscosity (η), an increase in the tube diameter (radius R) leads to faster filling of the tube by water. This occurs because, in narrow tubes with small diameters, the viscous resistance force dominates over the capillary force, resulting in slower fluid flow. Conversely, in wider tubes with larger diameters, the capillary force (driven by surface tension and contact angle) has a greater influence, while viscous resistance is reduced, leading to faster flow.

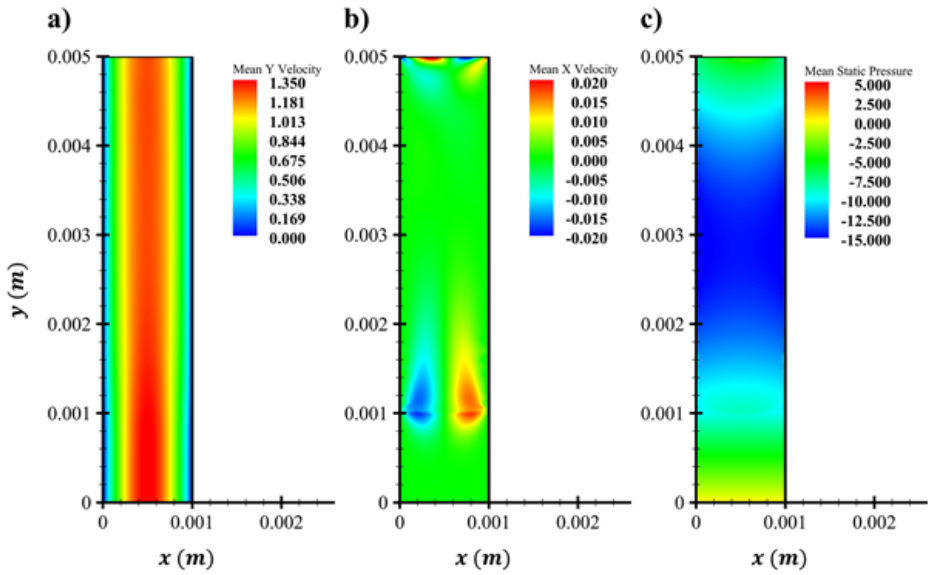

Figure 5: The contours of (a) mean y velocity; (b) mean x velocity; (c) mean static pressure of capillary tube.

Figure 5 illustrates the effects of varying CT diameters. In this figure, a fluid with a density of 0.001 kg/m^3—used as validation data with the L-W equation—was examined in three tubes with diameters of 0.5 mm, 1 mm, and 2 mm. Alongside each numerical study, the corresponding L-W equation curve for the respective diameter is plotted. Two key points can be drawn from this figure: The numerical model employed in this simulation demonstrates sufficient accuracy and validity in capturing the physics of capillary-driven water uptake in the tube. As the diameter increases (2 mm vs. 1 mm), the tube filling velocity increases, whereas a decrease in diameter (0.5 mm vs. 1 mm) leads to a reduction in filling velocity. The magnitude of this increase/decrease in filling velocity is approximately 98% (increase) and 49% (decrease), respectively. These observations are consistent with and well-predicted by the L-W equation. Figure 6 demonstrates the influence of diameter variation on the rising time of water with a density of 1000 kg/m^3 (representing water under standard conditions). The results from Figs. 6 and 7 exhibit strong agreement. Specifically, for water under standard conditions, the increase/decrease in tube filling time due to diameter variation is approximately 100% (increase) and 50% (decrease), respectively. Table 3 demonstrates the time-averaged uptake velocity of water at different heights for different tube diameters. The results of this table are consistent with the results of Figure 7. The increase/decrease in water uptake velocity due to diameter variation is

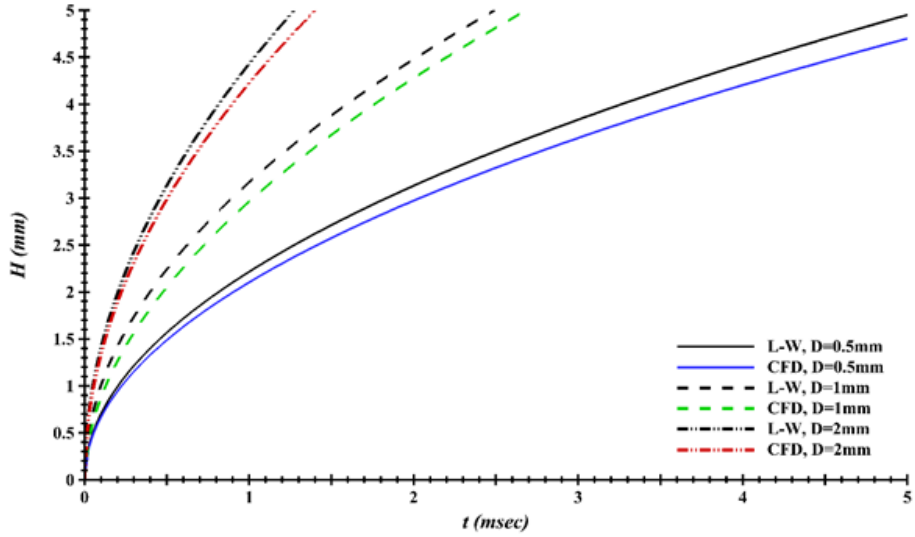

Figure 6: Fluid ($\rho = 0.001 \ \ kg/m^3$) uptake in the CT (CFD) with different tube diameters (0.5, 1, 2mm) via the L-W equation (L-W); the vertical and horizontal axes are represented as mm (millimeter) and $msec$ (millisecond).

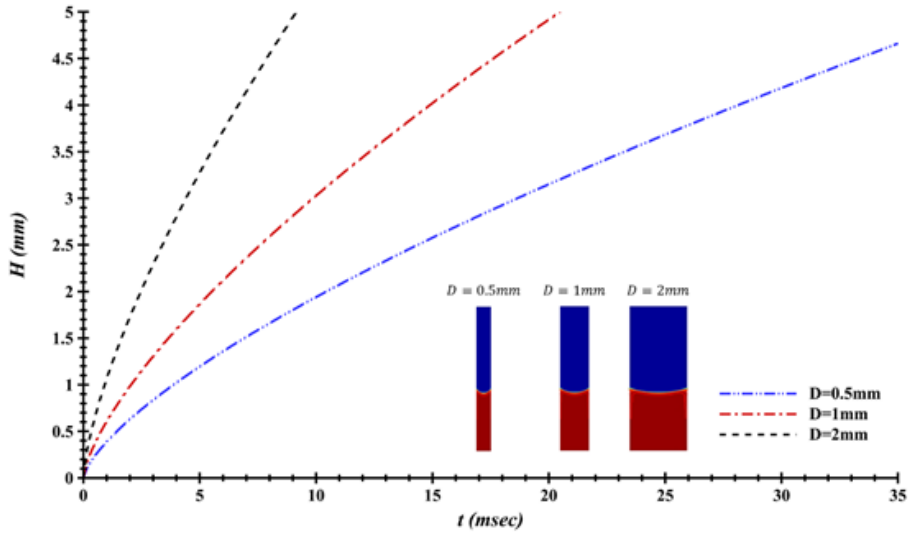

Figure 7: Water ($\rho = 1000 \ kg/m^3$) uptake in the CT with different tube diameters (0.5, 1, 2mm); the vertical and horizontal axes are represented as mm (millimeter) and $msec$ (millisecond).

approximately 100% (increase) and 50% (decrease), respectively.

Table 3: Time-averaged uptake velocity (m/s) of water at different heights for different tube diameters.

H (mm)	$D = 0.5$ mm	$D = 1$ mm	$D = 2$ mm
0	0.0000	0.0000	0.0000
1	0.3069	0.5800	1.2976
1.5	0.1162	0.2197	0.4915
2	0.1058	0.2000	0.4474
2.5	0.1230	0.2325	0.5200
3	0.1406	0.2658	0.5947
3.5	0.1428	0.2698	0.6037
4	0.1464	0.2767	0.6190
4.5	0.1442	0.2725	0.6096
5	0.1435	0.2713	0.6069

3.2 Surface tension study

To study the surface tension effects, assuming all other parameters remain constant (tube radius R, viscosity η, contact angle θ, and ρ fluid density), variations in surface tension force directly influence the kinetics of capillary flow. For better understanding, the L-W equation can be utilized. If the time derivative of the L-W equation ($h\,(t) = \sqrt{\frac{\gamma R cos\theta}{2\eta}t}$) has been taken, the instantaneous velocity of water uptake can be derived ($v = \frac{dh}{dt}$):

$$v = \frac{dh}{dt} = \frac{\gamma R cos\theta}{4\eta h} \tag{3.5}$$

From the above equation, it is evident that v is directly proportional to γ. This means that if γ increases, the instantaneous velocity of water uptake at any height h increases. Conversely, if γ decreases, the instantaneous velocity at any height h decreases.

The time required to reach a specific height (t) can be calculated from the main equation as follows:

$$t = \frac{2\eta h^2}{\gamma R\ cos\theta} \tag{3.6}$$

Here, t is inversely proportional to γ. In other words, if γ increases, the time required to reach height h decreases, and vice versa.

Figure 8 illustrates the capillary uptake of water in a tube under different surface tension forces. The water fluid under standard conditions experiences a

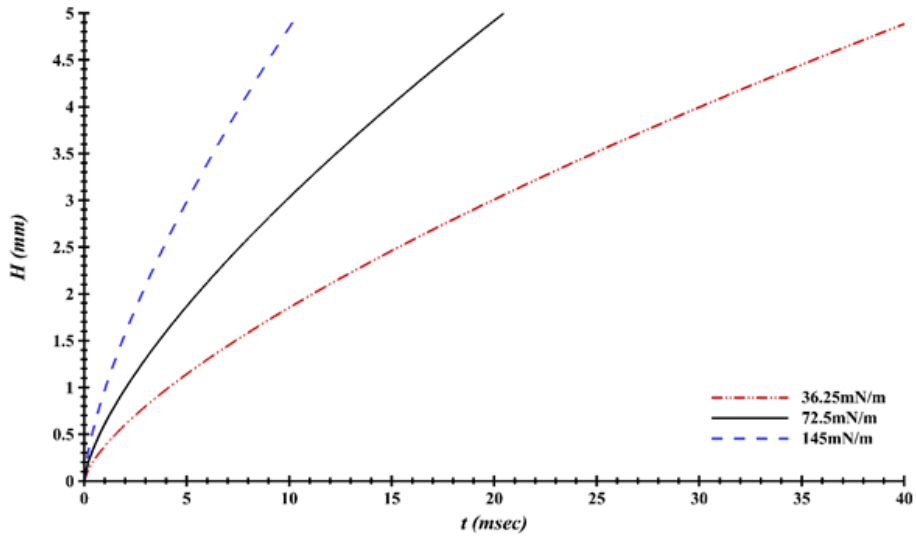

Figure 8: Water ($\rho = 1000\ kg/m^3$) uptake in the CT with different surface tension (36.25, 72.5, 145 mN/m); vertical and horizontal axes are represented as mm (millimeter) and $msec$ (millisecond).

surface tension of 72.5 mN/m, where in this section, two additional forces of 36.25 and 145 mN/m have also been investigated. In accordance with the presented physical analysis, with the increase of surface tension from 72.5 mN/m to 145 mN/m, approximately 50% of the CT filling time has been reduced. On the other hand, with a 50% decrease in surface tension from 72.5 mN/m to 36.5 mN/m, the tube filling time has doubled. Table reftab4 presents the time-averaged water uptake velocity and its dependence on surface tension variations. Although, according to the L-W equation, the effects of diameter change and surface tension on uptake velocity should be similar, but the percentage difference between corresponding points ranges from 1% to 12%. This discrepancy arises due to the influence of other parameters that are either not considered or minimally accounted for in the L-W equation. However, in simulations (approximating real-world conditions), these differences manifest due to the inertial force of the liquid column and dissipative effects.

3.3 Contact angle study

Based on the relationship derived in the previous section (eq. 2.4), it is expected that $v \propto cos\theta$ and $t \propto 1/cos\theta$. Therefore, with increasing cosine of the contact angle, the velocity and uptake time of water increase and decrease, respectively.

Table 4: Time-averaged uptake velocity (m/s) of water at different heights for different surface tensions.

H (mm)	$\gamma = 36.25$ mN/m	$\gamma = 72.5$ mN/m	$\gamma = 145$ mN/m
0	0	0	0
1	0.2872	0.5800	1.1351
1.5	0.1088	0.2197	0.4299
2	0.0990	0.2000	0.3914
2.5	0.1151	0.2325	0.4549
3	0.1316	0.2658	0.5202
3.5	0.1336	0.2698	0.5280
4	0.1370	0.2767	0.5415
4.5	0.1349	0.2725	0.5332
5	0.1343	0.2713	0.5309

It should be noted that as the contact angle increases and approaches 90 degrees, the cosine of the angle decreases, consequently leading to a reduction in velocity and an increase in uptake time of water, respectively.

As shown in Figure 9, which depicts the water uptake time in a CT, the reference angle was 55°, with two additional angles of 30°and 75° considered to study the effect of contact angle variation. In precise agreement with the theoretically derived relationship, the water uptake time at 75° shows a significant increase compared to 55°and 30°. This increase becomes particularly more pronounced when the tube filling time becomes longer due to the dominance of inertial effects. At the initial stage of water uptake movement in the CT and during short time periods, viscous effects dominate, and no significant difference is observed. However, as time progresses, the discrepancy becomes more substantial, ultimately resulting in the total tube filling time increasing from approximately 20 $msec$ at 55° to about 40 $msec$ at 75°. According to Table 5, the same behavior of velocity profile at each point for each contact angle is discernible, i.e. the inert water speeds up to the maximum value at the $h = 1mm$, then slows down to the minimum value at the top of CT. With an increase in contact angle from 30°to 75°, the velocity at each point of the velocity profile is higher for smaller angles. The sharp velocity reduction between $1.5 - 2$ mm heights is one of the indicators of significant inertial forces effects. After this sharp velocity attenuation, lazy velocity augmentation can be seen.

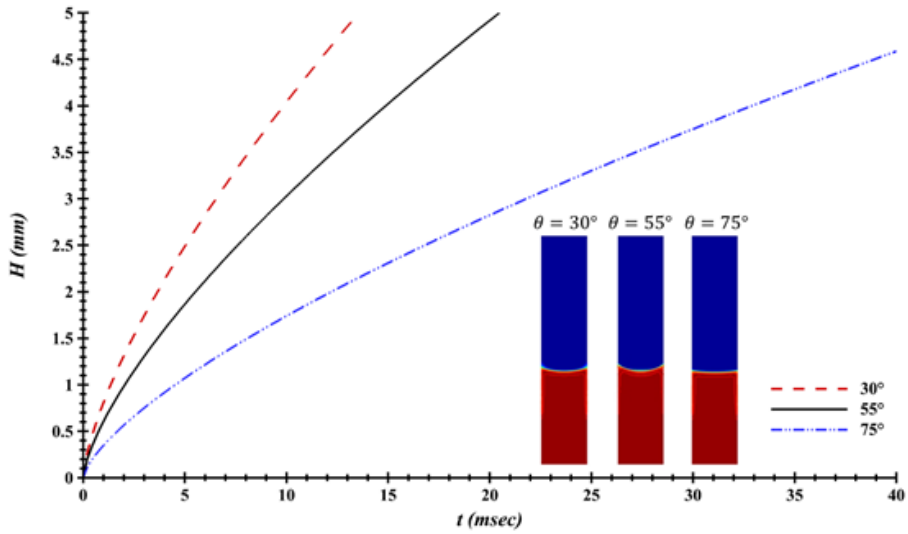

Figure 9: Water ($\rho = 1000\ kg/m^3$) uptake in the CT with different contact angles (30°, 55°, 75°); the vertical and horizontal axes are represented as mm (millimeter) and $msec$ (millisecond).

Table 5: Time-averaged uptake velocity (m/s) of water at different heights for different contact angles.

H (mm)	$\theta = 30°$	$\theta = 55°$	$\theta = 75°$
0	0.0000	0.0000	0.0000
1	0.8758	0.5800	0.2625
1.5	0.3317	0.2197	0.0994
2	0.3020	0.2000	0.0905
2.5	0.3510	0.2325	0.1052
3	0.4014	0.2658	0.1203
3.5	0.4074	0.2698	0.1221
4	0.4178	0.2767	0.1252
4.5	0.4114	0.2725	0.1233
5	0.4096	0.2713	0.1228

3.4 Gravity force study

The phenomenon of water ascent in CTs under gravitational acceleration ($-9.81\ m/s^2$) has been investigated in this section. In the classical L-W equation, derived from the Stokes equation, gravitational effects are not incorporated. This simplifying assumption motivate to examination of the influence of the gravitational force. The results demonstrated that accounting for gravitational force in the simulation affected the solution by approximately 2% during the initial phase (early stages of water ascent up to 2 mm height) and by nearly 5% over longer durations, resulting in flow deceleration and consequently increasing the tube filling time. However, this increase in filling time is negligible and can be disregarded, serving only to elevate computational costs. For engineering applications, the assumption of neglecting gravitational force may be considered valid based on the findings of this study. Furthermore, the meniscus profile exhibited minimal alteration.

3.5 Inclination angle Study

To investigate the effect of deformation on the meniscus profile and the duration of water uptake in a CT, two studies were conducted according to Figure 10, which illustrates the schematic geometry. The CT depicted in Figure 2, with an identical diameter and vertical length of 5 mm, was positioned at two inclination angles of $\beta = 45°$ and $\beta = 0°$, while maintaining similar boundary conditions, mesh structure, and time step settings as in previous studies. Also, for a more comprehensive understanding of water uptake in the inclined and horizontal CT, animations (incline CT and horizontal CT) of the entire simulations' duration have been provided, and they are included in the supplementary materials of the article. According to the mentioned animation and Figure 11 (which depicts Different moments of water uptake in incline ($\beta = 45°$) and horizontal ($\beta = 0°$) CT), in the initial moments of the solution (Figure 11(a) and incline CT animation), the distinct effects of contact angle and surface tension forces on the right and left halves of the tube are clearly observable. Specifically, the initial change in the curvature of the meniscus profile begins at the left half (Figure 11(b)) and gradually propagates to the right half. Until the meniscus profile stabilizes (Figure 11(c) and horizontal CT animation), a highly asymmetric curvature is evident at the onset of motion, which progressively diminishes in intensity, resulting in a relatively symmetric profile (the relatively symmetric stable meniscus profile is displayed in the zoomed-in view of Figure 11(f)). A noteworthy observation is that, unlike the vertical CT, in the 45-degree inclined CT, both halves of the meniscus curvature do not ascend simultaneously upon contact with the wall. Instead, the left half initially draws the fluid upward (Figure 11(b)), followed by

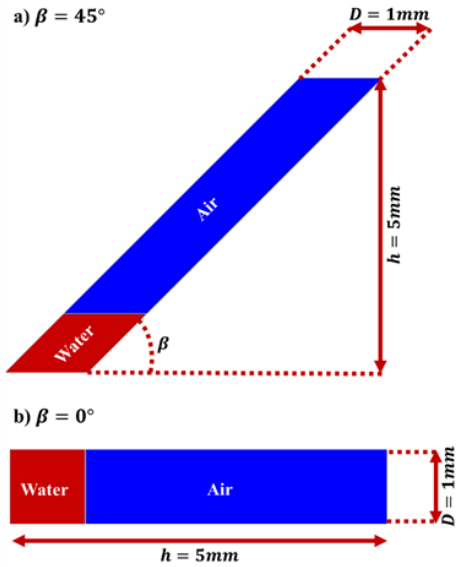

Figure 10: The schematic view of shape study on water uptake with different inclination angles, (a) $\beta = 45°$; (b) $\beta = 0°$

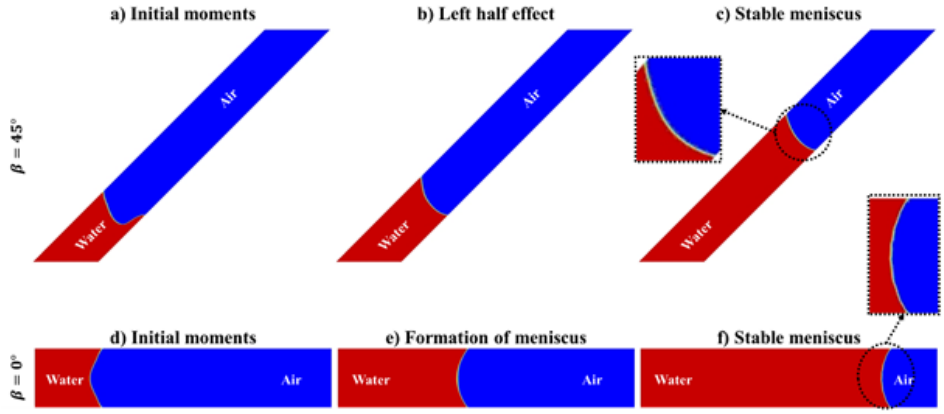

Figure 11: Different moments of water uptake in an incline ($\beta = 45°$) CT (a, b, c) and horizontal ($\beta = 0°$) CT (d, e, f), (a, d) initial moments; (b) Left half effect; (c, f) Stable meniscus; (e) formation of meniscus.

the right half, achieving a brief equilibrium before the cycle repeats. The primary reason for this phenomenon lies in the difference in contact angles due to the tube wall inclination, where the left half forms a smaller contact angle with the fluid compared to the right half.

Unlike the flow physics in an inclined tube, the meniscus behavior in horizontal (Figure 11(d, e, f)) and vertical tubes exhibits significant similarities. In contrast to an inclined CT, the contact angles in both halves of the CT are equal, and the symmetric meniscus profiles in vertical and horizontal CTs are analogous. At the onset of motion (Figure 11(d)) in the horizontal CT, the meniscus slope is more pronounced; however, as time progresses (Figure 11(e)) and the water advances toward the tube's end, the slope gradually diminishes (Figure 11(f)).

If the meniscus profile geometry has changed, it is particularly noteworthy that the tube filling time has not shown any significant difference compared to the vertical tube case, and the water has filled the tube in the same duration across all three case studies. Figure 12 illustrates the contour of mean static pressure (a, d), mean x velocity (b, e), and mean y velocity (c, f) for an incline ($\beta = 45°$) CT (a, b, c) and horizontal ($\beta = 0°$) CT (d, e, f). The behavior of the mean pressure variation in these two tubes is entirely different, and they exhibit distinct pressure distributions. The pressure distribution is asymmetric at the inlet and outlet of the inclined tube (Figure 12(a)), whereas it is perfectly symmetric in the horizontal tube (Figure 12(d)). A significant pressure increase is observed in the regions corresponding to the acute angle of the inclined tube, and a notable negative pressure is evident in the initial obtuse angle region of the inclined tube. This phenomenon is not observed in the horizontal tube (Figure 12(d)). The mean x velocity profile (in the flow direction) near the wall is relatively similar in both tubes (Figure 12(b, e)); however, the mean y velocity pattern (in the direction perpendicular to the flow) is entirely different in the horizontal tube (Figure 12(c, f)). The mean y velocity cores of equal magnitude and opposite direction (Figure 12(f)), featuring a symmetric structure, indicate a symmetric meniscus profile. These cores are one of the consequences of the surface tension force and the formation of a concave meniscus profile.

4. Conclusion

In the present study, using CFD techniques, the capillary action and fluid uptake in CT have been investigated. First of all, the model's validation has been done by the L-W equation and followed by a grid and time-step independence study. Parameters' effect study (i.e. fluid density, surface tension, contact angle, tube diameter, tube inclination angle, gravity force) on the capillary filling time, and

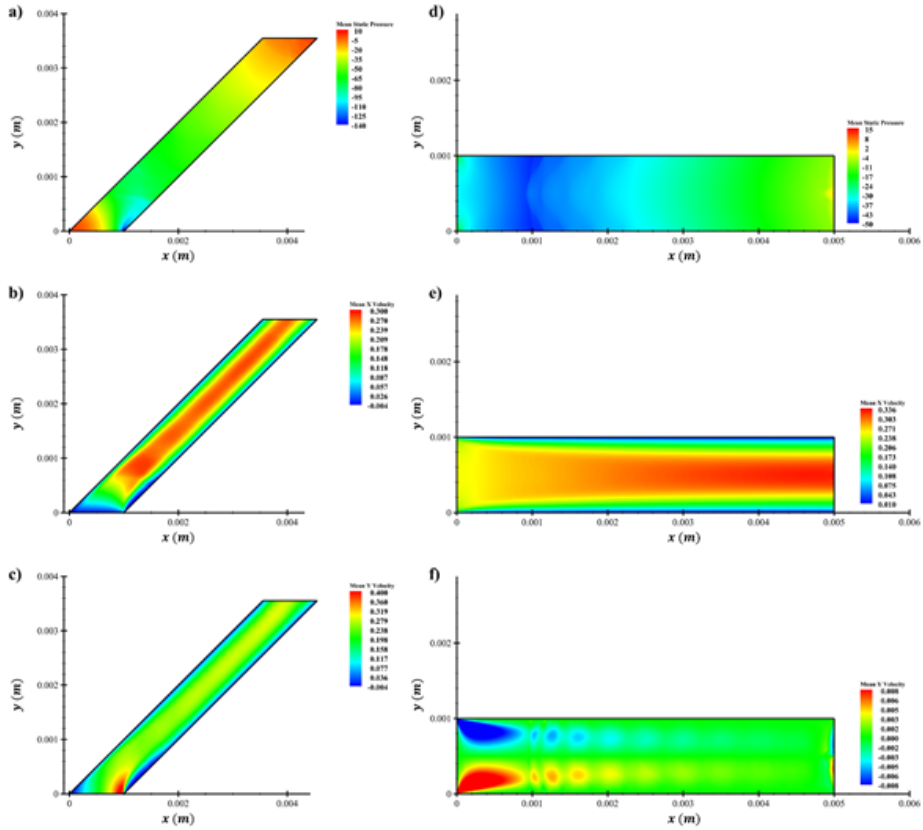

Figure 12: The contours of mean static pressure (a, d), mean x velocity (b, e), and mean y velocity (c, f) for an incline ($\beta = 45°$) CT (a, b, c) and horizontal ($\beta = 0°$) CT (d, e, f)

uptake velocity have been presented. To answer the main question of the research regarding which parameters influence the uptake capillary motion of water, the results demonstrate that density and viscosity significantly affect both the rising velocity and CT filling time. Furthermore, diameter, surface tension, and contact angle constitute additional influential parameters. While the tube's inclination angle affects the meniscus profile, gravitational effects may be considered negligible.

According to these, the following conclusions can be summarized:

- Increasing CT diameter significantly enhances filling velocity (approximately 98-100% increase for wider tubes) while decreasing diameter reduces velocity (approximately 49-50% reduction for narrower tubes), due to the dominant influence of capillary forces over viscous resistance in larger diameters, with strong agreement with theoretical predictions.

- Increasing surface tension (γ) from 72.5 mN/m to 145 mN/m reduces CT filling time by approximately 50%, while decreasing γ to 36.25 mN/m doubles the filling time, consistent with the L-W equation's predictions; however, simulations reveal deviations of 1-12% in uptake velocity attributed to unaccounted inertial forces and dissipative effects not fully captured by the L-W model.

- Increasing the contact angle (e.g., from 55° to 75°) significantly prolongs CT filling time by approximately 100% (20 ms to 40 ms) and reduces velocity monotonically at all profile points (30° to 75°), with inertial forces amplifying temporal discrepancies during extended filling and inducing sharp velocity attenuation at 1.5–2 mm height before gradual recovery.

- Simulations incorporating gravitational acceleration (-9.81 m/s^2) reveal that its omission in the classical L-W equation introduces minor flow deceleration, increasing CT filling time by approximately 2% during initial ascent ($\leq 2mm$ height) and $\sim 5\%$ over extended durations. However, these effects are negligible for engineering applications and computationally costly, with negligible meniscus alteration observed.

- Tube inclination angle (45°) induces transient asymmetric meniscus curvature and sequential fluid advancement in inclined capillaries due to contact angle disparity between halves, yet tube filling time remains unchanged compared to vertical orientations, with horizontal CT exhibiting meniscus symmetry akin to vertical tube despite initial slope variations.

This research aimed to perform computational fluid dynamics modeling of water uptake in a capillary tube due to surface tension and the capillary phenomenon,

and to identify the flow physics in this domain. For this purpose, a time-dependent, finite volume, parallelized code for an incompressible fluid with constant and Newtonian properties was used. Five geometries with different walls were selected for this study, and the results are as follows:

Neglecting inertial effects in computational fluid dynamics simulations leads to a fluid rising velocity consistent with the predictions of the Lucas-Washburn equation. If inertial effects are not neglected in the simulation, the deviation of the results from the Lucas-Washburn equation is evident from the beginning and becomes increasingly significant over time. In fact, it appears that as the tube length and the fluid's ascent time increase, the discrepancy with the theoretical Lucas-Washburn equation becomes more pronounced. This phenomenon occurs because although the Lucas-Washburn equation was derived for Poiseuille flow, its formulation neglects inertial effects, dissipative phenomena, and other forces.

To address the limitations of the present research, which include the millimeter scale and the exclusive use of water as the fluid, studying the flow physics of water uptake and the capillary phenomenon in micro- and nanotubes using computational fluid dynamics methods, and considering other solid phases dissolved in water, can be regarded as necessary recommendations and suggestions for future investigations.

5. Research limitations and future studies

Every numerical study faces challenges and limitations, one of the most significant being computational costs and restricted access to high-performance computing resources. With access to supercomputing facilities, one could employ a direct numerical simulation (DNS) model to study capillary phenomena and achieve an exact and accurate understanding. The application of machine learning algorithms, adaptive neuro fuzzy inference system (ANFIS), and artificial intelligence could enhance the speed and precision of examining more parameters while providing comprehensive insight into flow physics - this illuminates a path for future research. Conducting CFD simulations for fluids like human blood containing drugs for targeted delivery to cells becomes possible through coupled CFD-MD simulations, artificial intelligence, and machine learning methods.

Funding

This research is supported by the research grant of the Imam Khomeini International University (258968).

References

Abdul Aziz M. S., Abdullah M. Z., Khor C. Y., Jalar A., and Che Ani F. (2014), CFD modeling of pin shape effects on capillary flow during wave soldering, *International Journal of Heat and Mass Transfer,* **72**, 400–410.

Adibifard M., Nabizadeh A., and Sharifi M. (2020), Computational fluid dynamics to develop novel correlations for residual saturation of the displaced fluid in a capillary tube, *Journal of Molecular Liquids,* **299**, 112122.

Amarasinghe P. M., Anandarajah A., and Ghosh P. (2014), Molecular dynamic study of capillary forces on clay particles, *Applied Clay Science,* **88–89**, 170–177.

Bhangale K. P., and Deshmukh M. M. (2021), A review of the optimization of length of capillary tube for a vapor compression refrigeration system, *International Journal of Innovative Engineering and Science,* **6**(2), 1–7.

Bosanquet C. H. (1923), On the flow of liquids into capillary tubes, *The London, Edinburgh, and Dublin Philosophical Magazine and Journal of Science,* **45**(267), 525–531.

Bullard J. W., and Garboczi E. J. (2009), Capillary rise between planar surfaces, *Physical Review E,* **79**(1), 011604.

Cai J., Jin T., Kou J., Zou S., Xiao J., and Meng Q. (2021), Lucas-Washburn equation-based modeling of capillary-driven flow in porous systems, *Langmuir,* **37**(4), 1623–1636.

Caltagirone J. (2024), Modeling capillary flows by conservation of acceleration and surface energy, *International Journal of Multiphase Flow,* **171**, 104672.

Chen Q., and Zhou J. (2023), Investigating the validity of the Bosanquet equation for predicting the self-diffusivities of fluids inside nanotubes using equilibrium molecular dynamics simulations, *AIP Advances,* **13**(2), 025338.

Chikami S., Maeda S., Latag G. V., Yamamoto H., and Tōma S. (2024), Analysis of the hydration water on the surface of human hair using a combination of infrared absorption vibrational spectroscopy and multivariate curve resolution, *Surface and Interface Analysis,* **56**(9), 580–586.

Dimitrov D. I., Milchev A., and Binder K. (2007), Capillary rise in nanopores: Molecular dynamics evidence for the Lucas-Washburn equation, *Physical Review Letters,* **99**(5), 054501.

Dremin V., Volkov M., Margaryants N., Myalitsin D., Rafailov E., and Dunaev A. (2025), Blood flow dynamics in the arterial and venous parts of the capillary, *Journal of Biomechanics,* **179**, 112482.

Fadel H. A. (2014), Water treatment by fabric capillary action: New technique with ancient origins, *American Water Works Association,* **106**(8), 44–50.

Folch A. (2025), The plants of progress: Capillary action in plants, the drop-by-drop extraction of useful juices from certain trees, and autonomous capillary microfluidic devices, In *How the world flows: Microfluidics from raindrops to COVID tests* (pp. 153–170). Oxford Academic.

Freidooni F., Sohankar A., and Rastan M. R. (2021), Flow field around two tandem non-identical-height square buildings via LES, *Building and Environment,* **201**, 107985.

Freidooni F., Sohankar A., and Rastan M. R. (2024), Turbulent wake of two non-identical-height tandem cantilevered prisms: Sheltering effect, *Ocean Engineering,* **304**, 117749.

Fries N., and Dreyer M. (2008), The transition from inertial to viscous flow in capillary rise, *Journal of Colloid and Interface Science,* **327**(1), 125–128.

Gaulke D., and Dreyer M. E. (2015), CFD simulation of capillary transport of liquid between parallel perforated plates using FLOW-3D, *Microgravity Science and Technology,* **27**(4), 261–271.

Gründing D., Bansch E., and Warncke E. (2020), A comparative study of transient capillary rise using direct numerical simulations, *Applied Mathematical Modelling,* **86**, 142–165.

Joly L. (2011), Capillary filling with giant liquid/solid slip: Dynamics of water uptake by carbon nanotubes, *The Journal of Chemical Physics,* **135**(21), 214705. https://doi.org/10.1063/1.3664622.

Jurin J. (1718), An account of some experiments shown before the Royal Society; with an enquiry into the cause of some of the ascent and suspension of water in capillary tubes, *Philosophical Transactions of the Royal Society of London,* **30**(355), 739–747.

Jurin J. (1719), An account of some new experiments, relating to the action of glass tubes upon water and quicksilver, *Philosophical Transactions of the Royal Society of London,* **30**(363), 1083–1096.

Khunte N. K., and Mishra R. (2022), ANSYS CFX, CFD analysis: Helical coiled capillary tube, *International Journal of Mechanical Engineering,* **7**(4), 1–5.

Koźluk M., Klamka M., Remer M., Rutkowski M., and Bobinski T. (2025), Displacement flow inside a capillary tube - The impact of boundary conditions on the dynamic contact angle, *International Journal of Multiphase Flow,* **192**, 105338.

Krajnović S. (2011), Flow around a tall finite cylinder explored by large eddy simulation, *Journal of Fluid Mechanics,* **676**, 294–317.

Krishna R., and van Baten J. M. (2012), Investigating the validity of the Bosanquet formula for estimation of diffusivities in mesopores, *Chemical Engineering Science,* **69**(1), 684–688.

Kubochkin N., and Gambaryan-Roisman T. (2022), Capillary-driven flow in corner geometries, *Current Opinion in Colloid & Interface Science,* **59**, 101575.

Legait B. (1983), Laminar flow of two phases through a capillary tube with variable square cross-section, *Journal of Colloid and Interface Science,* **96**(1), 28–38.

Li X., Zhao Y., and Zhao C. (2021), Applications of capillary action in drug delivery, *iScience,* **24**(6), 102810.

Liu X., Huang Y., and Li G. (2016), CFD simulation of capillary rise of liquid in cylindrical container with lateral vanes, *International Journal of Modern Physics Conference Series,* **42**, 1660154.

López A. W., Bruno A. W., and Nadimi S. (2021), CFD modelling of the effect of capillary pressure on retention behavior of water menisci at inter-particle contacts, *EPJ Web of Conferences,* **249**, 09008.

Lucas R. (1918), Rate of capillary ascension of liquids, *Kolloid-Zeitschrift,* **23**(1), 15–22.

Mark S., and Boyer H. (2020), Spatial limit of CFD model at nanometer scale geometry: Part I: Capillary flow, *European Journal of Engineering and Technology Research,* **5**(7), 795–799.

Martic G., Gentner F., Seveno D., Coulon D., De Coninck J., and Blake T. D. (2002), A molecular dynamics simulation of capillary imbibition, *Langmuir,* **18**(21), 7971–7976.

Mu W., and Cao L. (2024), Water absorption dynamics in medical foam: Empirical validation of the Lucas-Washburn model [Preprint], *arXiv.*

Panter J. R., Konicek A. R., King M. A., Hodes M., and Wilkinson A. R. (2023), Rough capillary rise, *Communications Physics,* **6**(1), 44.

Quéré D. (1997), Inertial capillarity, *Europhysics Letters,* **39**(5), 533–538.

Quéré D., Raphaël É., and Ollitrault J. (1999), Rebounds in a capillary tube, *Langmuir,* **15**(10), 3679–3682.

Schönfeld F., and Hardt S. (2009), Dynamic contact angles in CFD simulations, *Computers & Fluids,* **38**(4), 757–764.

Stüben K. (2001), Introduction to algebraic multigrid, In U. Trottenberg, C. W. Oosterlee, & A. Schüller (Eds.), *Multigrid.* Academic Press.

Ubbink O., and Issa R. I. (1999), A method for capturing sharp fluid interfaces on arbitrary meshes, *Journal of Computational Physics,* **153**(1), 26–50.

Washburn E. W. (1921), The dynamics of capillary flow, *Physical Review,* **17**(3), 273–283.

Weiss J. M., Maruszewski J. P., and Smith W. A. (1997), Implicit solution of the Navier-Stokes equations on unstructured meshes (AIAA Report No. 97-2103), 13th *AIAA Computational Fluid Dynamics Conference.*

Ziarani N. N., Cook M. J., Freidooni F., and O'Sullivan P. D. (2023), The role of near-façade flow in wind-dominant single-sided natural ventilation for an isolated three-storey building: An LES study, *Building and Environment,* **235**, 110210.

Zhang L., Cui Z., Cao Q., Liang S., Liu Y., and Ma X. (2022), Molecular dynamics study of spontaneous capillary flow and heat transfer in nanochannels, *International Communications in Heat and Mass Transfer,* **137**, 106228.